J. Fluid Mech. (2013), *vol.* 727, *pp.* 30–55. © Cambridge University Press 2013
doi:10.1017/jfm.2013.230

Mode C flow transition behind a circular cylinder with a near-wake wire disturbance

I. Yildirim, C. C. M. Rindt† and A. A. van Steenhoven

Energy Technology Section, Faculty of Mechanical Engineering, Eindhoven University of Technology, Den Dolech 2, 5612 AZ, Eindhoven, The Netherlands

(Received 20 April 2012; revised 8 April 2013; accepted 1 May 2013; first published online 14 June 2013)

The three-dimensional transition of the flow behind a circular cylinder with a near-wake wire disturbance has been investigated experimentally. The asymmetric placement of a wire in the near-wake region of the cylinder causes an unnatural mode of shedding to occur, namely mode C. We performed flow visualization and particle image velocimetry (PIV) experiments to investigate the influence of the wire on various properties of the flow, such as the dynamics of the streamwise secondary vortices. Experiments were performed at the Reynolds number range of $Re = 165$–300. From these experiments, it can be concluded that mode C structures are formed as secondary streamwise vortices around the primary von Kármán vortices. The spanwise wavelength of those mode C structures is determined to be approximately two cylinder diameters. The presence of the wire also triggered the occurrence of period doubling in the wake. Each new set of mode C structures is out of phase with the previous set, i.e. doubling the shedding period. This period-doubling phenomenon is due to a feedback mechanism between the consecutively shed upper vortices.

Key words: vortex instability, vortex shedding, wakes/jets

1. Introduction

Due to its simple geometry, the flow around circular cylinders has become a central topic in much research. A lot of effort has been made to explain the physics of circular cylinder wake dynamics by Gerrard (1966, 1978) and Green & Gerrard (1993). They showed that vortex shedding for low Reynolds numbers can be characterized by vortex splitting and high shear stress occurring in the near wake. Unal & Rockwell (1988) investigated the near-wake vortex formation in the context of absolute instability and showed that the shear layer separating from the cylinder shows an exponential variation of fluctuating kinetic energy with distance downstream of the cylinder.

However, the above-mentioned studies were limited to the two-dimensional aspects of the flow. The three-dimensional aspects of wake flows behind circular cylinders are thoroughly reviewed and discussed by Williamson (1996*a*,*b*). The laminar vortex shedding regime extends from a Reynolds number of 49 to 140–194, and the flow regime between $Re = 190$ and 260 is denoted as the three-dimensional wake transition regime. This regime is associated with two modes of shedding, modes A and B.

† Email address for correspondence: c.c.m.rindt@tue.nl

https://doi.org/10.1017/jfm.2013.230 Published online by Cambridge University Press

The stability characteristics of mode A and B transitions have been investigated by Williamson (1992, 1996*a*), Leweke & Williamson (1998) and Thompson, Leweke & Williamson (2001). They noted that the origin of the instability arises from an elliptic instability of vortex cores for mode A and from a hyperbolic instability in the braid region for mode B. Another approach to describing the onset of the vortex loops is provided by Brede, Eckelmann & Rockwell (1996). They identified a centrifugal instability of the braid region between the primary vortices using the analysis of particle image velocimetry (PIV) data. The conclusion of Brede *et al.* (1996) was that the interaction of the primary vortices in this braid region is the main amplification mechanism. They concluded that mode B vortices originate from the instability of the separating shear layer in the near wake, which results in a different topology of the mode B vortices compared with those in mode A. The stability characteristics of these modes have been thoroughly investigated numerically by Barkley & Henderson (1996), Henderson (1996, 1997) and Barkley, Tuckerman & Golubitsky (2000).

It is shown in various studies that under the influence of 'disturbances', cylinder wake flows exhibit different flow structures. For example, Ren, Rindt & van Steenhoven (2006) showed that by heating the cylinder, a different transition regime can be found, denoted as mode E. Strykowski & Sreenivasan (1990) studied the mechanism of suppression of vortex shedding by proper placement of a second, much smaller, cylinder in the near wake of the main cylinder for low Reynolds numbers in the laminar, two-dimensional periodic flow regime. The configuration at low Reynolds numbers was further studied by Mittal & Raghuvanshi (2001), Dipankar, Sengupta & Talla (2007), Kuo, Chiou & Chen (2007) and Marquet, Sipp & Jacquin (2008). Yildirim, Rindt & van Steenhoven (2010) studied the effect of a thin control wire on the wake properties for laminar two-dimensional wake flow, investigating its vortex dynamics and vortex shedding process. Zhang *et al.* (1995) studied the influence of the presence of a wire in the vicinity of a cylinder on transition, also the focus of the present study, and characterized the wake transition regime as mode C, which shows different properties compared to modes A and B.

The first evidence of mode C appeared in the computations and experiments of Zhang *et al.* (1995), when a tiny wire was placed close to a circular cylinder. In their flow visualization experiments, they observed that mode C transition takes place over a Reynolds number range of $170 < Re < 270$. Numerical simulations at $Re = 210$ displayed a spanwise periodicity of 1.8 cylinder diameters. Another flow type in which mode C transition takes place is the flow behind circular rings. Using Floquet stability calculations, Sheard, Thompson & Hourigan (2003) identified this mode as the primary transition mode in the aspect ratio (AR) range of $3.9 \lesssim AR \lesssim 8$, with a spanwise wavelength of approximately 1.7 ring cross-section diameters. Further nonlinear characterization of mode C was undertaken by Sheard, Thompson & Hourigan (2004), using direct numerical simulations. They showed that for the flow past a ring with $AR = 5$, mode C instability produces a period doubling in the wake through supercritical and non-hysteretic transition. Subsequently, Sheard *et al.* (2005*b*) provided additional computational results and first experimental observations about the existence of the subharmonic mode C. Later, Sheard, Thompson & Hourigan (2005*a*) showed that the period-doubling nature of the wake is maintained by a cycle of convection of the perturbation vorticity from the near wake.

Carmo *et al.* (2008) also found mode C in the wake transition of the flow around staggered arrangements of equi-diameter circular cylinders for different relative positions. The structure and onset characteristics of mode C were analysed using linear and nonlinear stability analyses as well as direct numerical simulations. They

https://doi.org/10.1017/jfm.2013.230 Published online by Cambridge University Press

showed that mode C appears in the near wake of the downstream cylinder, with an intermediate spanwise wavelength between modes A and B that has a period-doubling character.

Detailed numerical investigations on mode C transition date back for more than two decades. One of the first studies using a high-order accurate direct numerical simulation of the Navier–Stokes equations was by Karniadakis & Triantafyllou (1992), who observed a mode C–like scenario by forcing a $\pi/2D$ periodicity in spanwise direction. Noack & Eckelmann (1994) employed a low-dimensional Galerkin method and found that the periodic solution becomes unstable at $Re = 170$ due to a perturbation with a spanwise wavelength of 1.8 diameters. However, relatively little attention has been devoted to the experimental investigation of the period-doubling nature of a wire-disturbed circular cylinder wake in mode C transition. The motivation behind the present study is to investigate the wake flow for the wired-cylinder case in the transition regime, verifying mode C type transition, examining its period-doubling character and establishing a physical explanation for the existence of period doubling.

First, the general characteristics of mode C transition at $Re \geqslant 180$ are determined in various ways. The flow visualization experiments illustrate the global picture of the phenomena and provide a global view of the physics of wake transition. The point velocity analysis provides information about the local flow characteristics and the period-doubling nature of the wake. Processing the point velocity data leads to several other characteristic properties of the mode C wake, such as phase plots, power spectra and Strouhal numbers.

Secondly, to understand the physical mechanism of the period-doubling character of the wake, the instantaneous vorticity patterns of the primary and secondary vortices are shown using the PIV vector fields of the near wake. Image sequences from flow visualization experiments are used to analyse the time evolution of secondary vortices. The overall analysis of the physics of the wake and the feedback mechanism of the vortices provides an insight into the origin of the period-doubling character of the mode C transition.

The plan of this paper is as follows. The experimental set-up is described in § 2. Section 3 describes the general characteristics of mode C transition in a wire-disturbed circular cylinder wake. In § 4, the evolution of near-wake vorticity patterns is presented and the period-doubling nature of the vortex shedding is shown. The physical formation mechanism for period doubling in the mode C wake is then presented in § 5. Finally, § 6 summarizes the findings and the discussion.

2. Experimental methodology

The experiments are performed in a towing tank with dimensions of $L \times W \times H = 500\ \text{cm} \times 50\ \text{cm} \times 75\ \text{cm}$ (Kieft *et al.* 2003). The towing tank walls are made of 15 mm thick single-piece glass, which provides optical accessibility from all directions. The test model is mounted on a moving carriage system, which is placed on the top of the sidewalls.

The experimental model is a circular cylinder with a diameter of $D = 15$ mm and a length of $L = 48$ cm. It is placed between circular end plates in order to force parallel shedding. In order to trigger mode C instability, a wire with a diameter of $d = 0.15$ mm is placed in the near wake. The ratio of the diameter of the cylinder to that of the wire is $D/d = 100$. The position of the wire is chosen in accordance with the work of Zhang *et al.* (1995), and is $(x/D, y/D) = (0.75, 0.75)$ relative to the centre of the cylinder, as shown in figure 1.

https://doi.org/10.1017/jfm.2013.230 Published online by Cambridge University Press

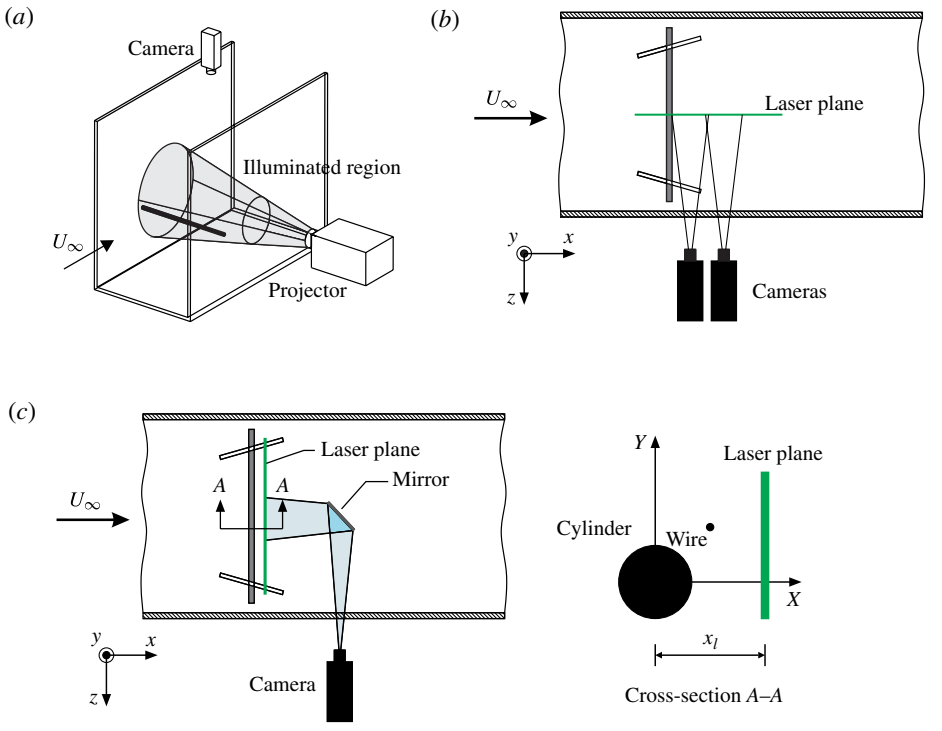

FIGURE 1. (Colour online) The measurement configurations. (*a*) The three-dimensional flow visualization configuration. (*b*) The side-view configuration. (*c*) The back-view configuration.

Figure 1 shows the three different measurement configurations that are used throughout the experiments. The first configuration is used for the three-dimensional flow visualization experiments (see figure 1(*a*)). The flow field behind the cylinder is illuminated using a slide projector. A camera is placed at the top of the set-up to record the images.

Figure 1(*b*) illustrates the second configuration, which is used for the investigation of the evolution of the primary, i.e. spanwise, vortices. This configuration is used for both flow visualization experiments and PIV measurements. The flow field is illuminated by a vertical laser sheet in the *XY*-plane, with a thickness of 3 mm. In the PIV experiments, the images are recorded synchronously with two side-by-side cameras to cover a larger field of view. The data obtained from the two-camera configuration are combined in the post-processing stage.

The third configuration is used for the investigation of the evolution of the secondary, i.e. streamwise, vortices. The layout of this configuration is shown in figure 1(*c*). The laser plane is located in the *YZ*-plane, with a thickness of 3 mm and its downstream position indicated as x_l. The images are recorded through a mirror placed downstream of the wake. The size of the mirror is 100 mm × 100 mm and it is placed at an angle of 45° with respect to the free-stream direction. The effect of the mirror on vortex shedding is evaluated using top-view flow visualization experiments. The results show that when the mirror centre is located $x_m = 16D$ downstream of the cylinder, clear parallel shedding is seen and at this position, the generation of secondary vortices is not affected by the mirror.

https://doi.org/10.1017/jfm.2013.230 Published online by Cambridge University Press

For the flow visualization experiments, the electrolytic tin-precipitation method was used (Honji, Taneda & Tatsuno 1980). This method is based on the generation of insoluble small particles on the surface of the model (Maas, Rindt & van Steenhoven 2003). Those particles are illuminated by a light source and their images are recorded by a camera. In the current set-up, the cylinder was covered by very thin tin-foil (70 μm) and that tin-foil was connected to an electrolysis set-up as the anode end. The cathode was placed at a downstream position where it did not disturb the flow. Very small tin hydroxide particles ($O(1\ \mu m)$) were then generated on the surface of the tin sheet by applying a voltage difference between the anode and the cathode. When the cylinder was pulled through the water, those particles detached from the surface and followed the flow.

The quantitative evaluation of the flow was done by using PIV. For this purpose, the water in the towing tank was seeded with Polyamid particles having a diameter of 20 μm. The flow was illuminated by using a Nd–Yag laser and the images were captured by an 12 bit camera with 1600 × 1200 pixels resolution and a 30 Hz frame rate. The camera fields of view in both the side-view and the back-view experiments were close to each other and corresponded to approximately $(S_x, S_y) \approx (7.3D, 5.5D)$ and $(S_y, S_z) \approx (5.2D, 6.9D)$ in terms of cylinder diameters, respectively. However, in the side-view experiments two cameras in a side-by-side arrangement were used to cover a larger field of view, which resulted in a field of view of approximately $(S_x, S_y) \approx (14.1D, 5.5D)$. The remaining recording parameters were the same in both types of experiment.

The water temperature was measured before every experiment to accurately calculate the kinematic viscosity value. This kinematic viscosity value, along with the desired Reynolds number, were used to calculate the corresponding free-stream velocity. The experiments were conducted at flow velocities ranging from 6 to 16 mm s^{-1}, corresponding to Reynolds numbers of 100–250 based on the diameter of the cylinder.

3. The general characteristics of mode C transition

3.1. *An overview by means of flow visualization experiments*

As a first step, the influence of a wire on the cylinder wake flow was investigated by three-dimensional flow visualizations, which revealed the general physics of the mode C structures in the transition regime. The global effects of a wire on the laminar wake transition of a circular cylinder are shown in figure 2, which contains snapshots taken with the camera placed on top of the set-up (see figure 1(*a*)). The free-stream velocity is in the positive X-direction and the camera axis is in the negative Y-direction in the global coordinate system. The original images were recorded by a digital camera and subsequently processed by image processing software. Each snapshot in the figure represents the vortex shedding phase at which the upper von Kármán vortex starts to form. In the snapshots, von Kármán vortices, i.e. primary vortices, are aligned along the cylinder axis, while the mode C vortices, i.e. secondary vortices, are formed between the primary vortices aligned in the streamwise direction.

The results in figure 2 clearly show the wake transition structure in the case of a wire-disturbed circular cylinder wake. No apparent three-dimensional vortical structures are present for $Re = 165$. However, for $Re \geqslant 180$, fine-scale dye structures appear in the wake connecting upper and lower primary vortices, indicating the presence of three-dimensional vortical structures. It is obvious that the critical Reynolds number for the transition, Re_{crit}, lies between $Re = 165$ and $Re = 180$. The Reynolds number for the onset of mode C instability is given as $Re = 170$

https://doi.org/10.1017/jfm.2013.230 Published online by Cambridge University Press

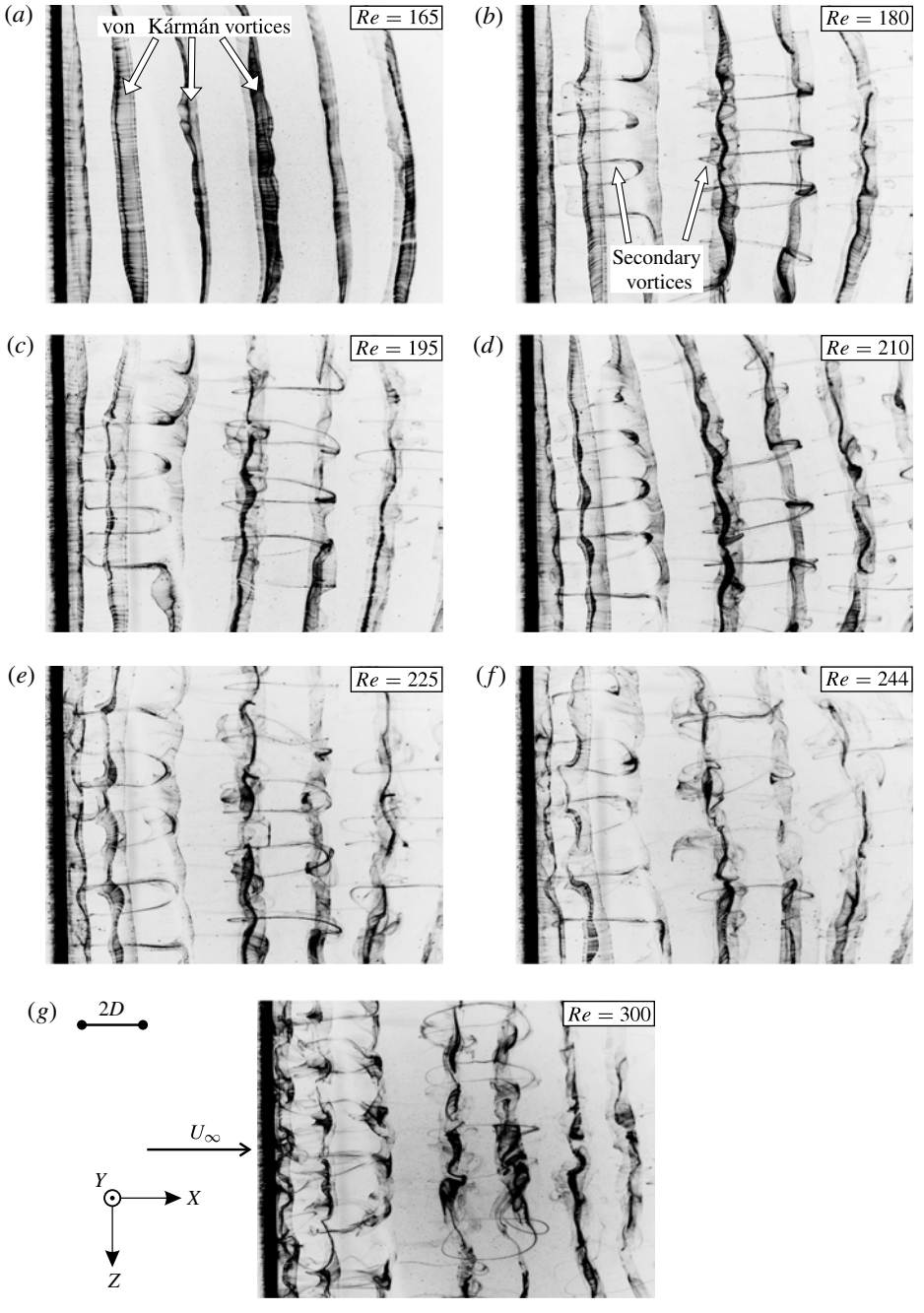

FIGURE 2. Top-view visualizations of the circular cylinder wake flow under the influence of a near-wake wire. Each picture is an instantaneous snapshot of the flow state taken at the corresponding Reynolds number. The flow direction in the pictures is from left to right.

https://doi.org/10.1017/jfm.2013.230 Published online by Cambridge University Press

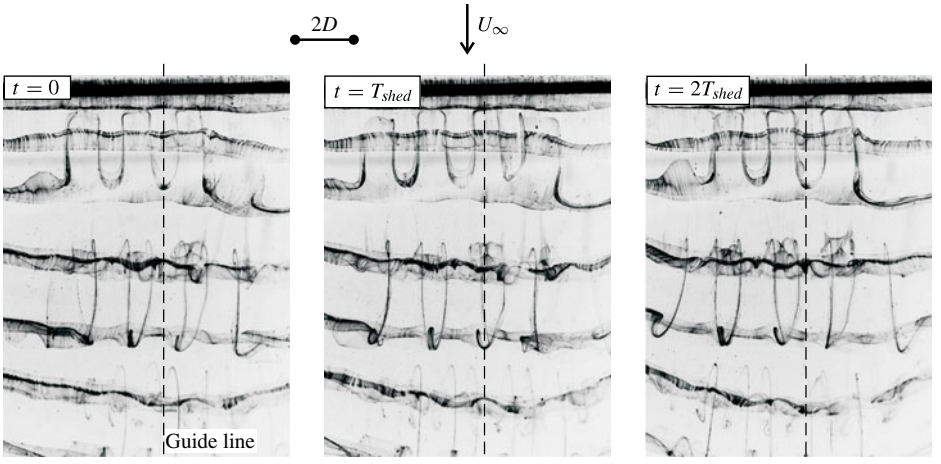

FIGURE 3. A top-view visualization of mode C structures at $Re = 195$. The flow direction in the pictures is from top to bottom.

by Zhang *et al.* (1995). However, the experimental set-up and methods used in this study did not allow an accurate determination of Re_{crit}.

The snapshots in figure 2 show that the formed three-dimensional structures are actually secondary streamwise vortices around the primary von Kármán vortices. These secondary structures indicate the presence of mode C type instability in the wake transition regime (see Zhang *et al.* 1995). They are uniformly distributed along the span of the cylinder, with a spanwise wavelength of $\lambda_z \approx 2D$. They are formed in the near wake and continue to exist in the far wake too.

The Reynolds number range of the experiments covers both the mode A and B regions of natural vortex shedding. Therefore, the results presented in figure 2 indicate the replacement of natural shedding modes with a forced shedding mode (mode C) in the Reynolds number range of 180–300. In this range, mode C structures get more disordered with increasing Reynolds number. However, unlike the natural wake transition, there is no drastic change in the vortex structure with increasing Reynolds number. When compared to the other shedding modes (Williamson 1996*a*; Ren *et al.* 2006), the differences in the wake structures suggest that the physical mechanism of formation is also altered by the wire.

Figure 3 shows the image sequence taken during the experiments for $Re = 195$. The cylinder is positioned at the top and the flow direction is from top to bottom. The time difference between each successive snapshot from left to right in the figures is one shedding period, which is denoted as T_{shed}. Examination of the instantaneous image sequence in figure 3 reveals an interesting feature of the mode C transition. In both the left and middle snapshots, the wake behind the cylinder has the same three-dimensional structures, but with a shift of approximately one cylinder diameter in spanwise position. The structures that appear on the line in the left snapshot appear on the line again after two shedding periods. So, effectively, the period of mode C has become two shedding cycles. This is an indication that the mode C transition has a period-doubling character, with each set of secondary vortices out of phase with the previous set. Period-doubling behaviour is observed in all of the flow visualization experiments in the wired-cylinder transition regime. However, this behaviour has been observed neither in non-wired-cylinder nor in heated-cylinder wake transitions.

https://doi.org/10.1017/jfm.2013.230 Published online by Cambridge University Press

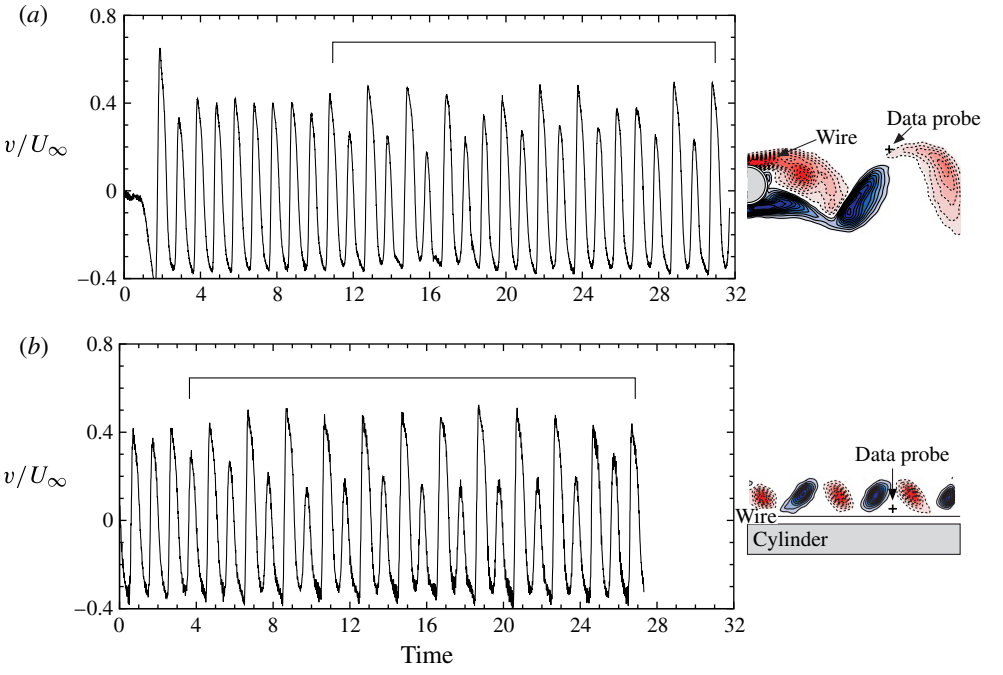

FIGURE 4. (Colour online) The time trace of the cross-stream velocity component v in two different experiments. (*a*) *XY*-plane PIV experiments, $Re = 180$; the data probe point is $(x/D, y/D) = (4.5, 1)$, (*b*) *YZ*-plane PIV experiments, $Re = 180$; the data probe point is $(x/D, y/D) = (4.5, 1)$. The *Z*-coordinate of the data point is selected to be between two secondary vortices. The time axis is non-dimensionalized with the corresponding shedding periods of each experiment.

3.2. *Point velocity characteristics*

Further analysis of the mode C wake transition is carried out by examining point velocity data in the near wake. The velocity data are obtained from PIV experiments by placing data probes at specific locations and tracing the data through consecutive vector fields. The velocity fluctuations in the wake identify the distinct characteristic properties of the mode C transition.

Figure 4 shows two cross-stream velocity signals at $Re = 180$, but obtained from different PIV experiments. Figure 4(*a*) represents data from *XY*-plane and figure 4(*b*) from *YZ*-plane measurements. The locations of the data probes are shown next to the corresponding graphs. In both cases, the flow needs time to develop to a more or less periodic state. The periodic states are indicated by the long braces.

3.2.1. *'High-peak–low-peak' velocity signal*

Figure 4 presents the typical 'high-peak–low-peak' velocity–time signal. This pattern is much more clear in figure 4(*b*) than in figure 4(*a*) due to the data probe locations between the two secondary vortices, where their effect on the cross-stream velocity is at a maximum.

The physical explanation for this 'high-peak–low-peak' pattern can be understood by considering the vorticity of the secondary vortices concentrated in point vortices, as shown in figure 5. If a point, p, lies on the mid-line of a vortex pair, as shown in figure 5(*a*), then the velocity at point p, v_p, can be calculated as the total velocity v_i

https://doi.org/10.1017/jfm.2013.230 Published online by Cambridge University Press

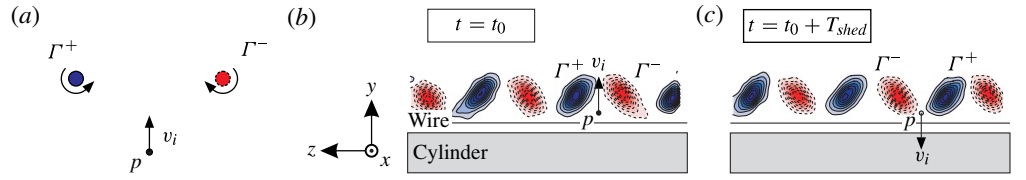

FIGURE 5. (Colour online) An analysis of the 'high-peak–low-peak' velocity profile in the mode C wake. (*a*) The point vortex model. (*b*) The upwards induced velocity, $v_i > 0$, due to secondary vortices. (*c*) The downwards induced velocity, $v_i < 0$, due to secondary vortices. v_{VK} is the vertical velocity component induced by von Kármán vortices and $v_{VK} > 0$. The blue (solid line) and red (dashed line) denote the positive and negative streamwise vorticities, respectively: (*a*) $v_p = v_i$; (*b*) $v_p = v_{VK} + v_i$; (*c*) $v_p = v_{VK} - v_i$.

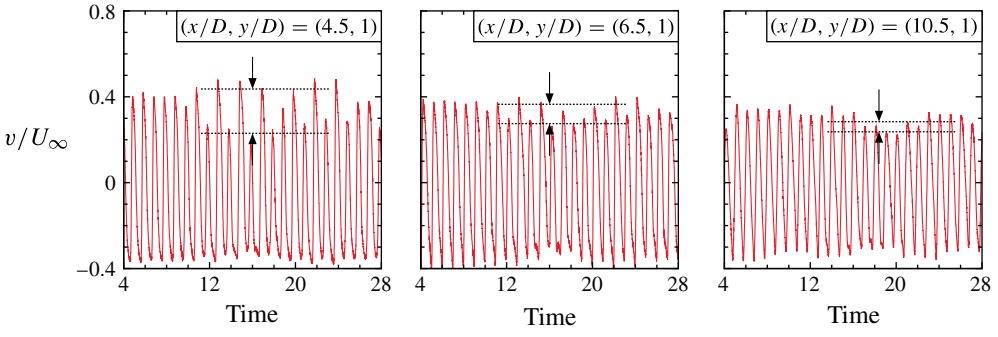

FIGURE 6. (Colour online) The downstream variation of the vertical velocity v in the upper half of the wake at $Re = 180$.

induced by the two counter-rotating point vortices of equal strength, Γ^- and Γ^+. Assuming now that point p lies between two secondary vortices in the mode C wake, as shown in figure 5(*b*,*c*), v_p contains two components; the induced velocity of the primary von Kármán vortices, v_{VK}, and that of the secondary vortices, v_i. At the vortex shedding time $t = nT_{shed}$, when the secondary vortices are at their uppermost position, v_{VK} is always positive, $v_{VK} > 0$.

As seen in figure 5(*b*,*c*), the vorticity of the secondary vortices changes sign after every period T_{shed}, which also affects the direction of the induced velocity v_i at *point p*. Hence, $v_p = v_{VK} + v_i$ at t_0 corresponds to the 'high peak' in the velocity signal and $v_p = v_{VK} - v_i$ at $t_0 + T_{shed}$ to the 'low peak'.

The above discussion shows that the difference between the 'high' and 'low' peaks in the velocity signal is due to the induced velocity of the secondary vortices, which changes sign in every shedding cycle. Figure 6 shows that this difference is decreasing in the streamwise direction. This suggests that the induced velocity v_i, and hence the vortex strengths of the secondary vortices, is decreasing and that the cross-stream velocity component is converging to the value of v_{VK}.

3.2.2. *Phase plots*

The analysis of the point velocity data showed that the mode C transition regime exhibits a unique repetitive 'high-peak–low-peak' velocity signal pattern due to the secondary mode C vortices, which change sign every vortex shedding cycle. The time difference between the consecutive high peaks (or low peaks) is twice the period

https://doi.org/10.1017/jfm.2013.230 Published online by Cambridge University Press

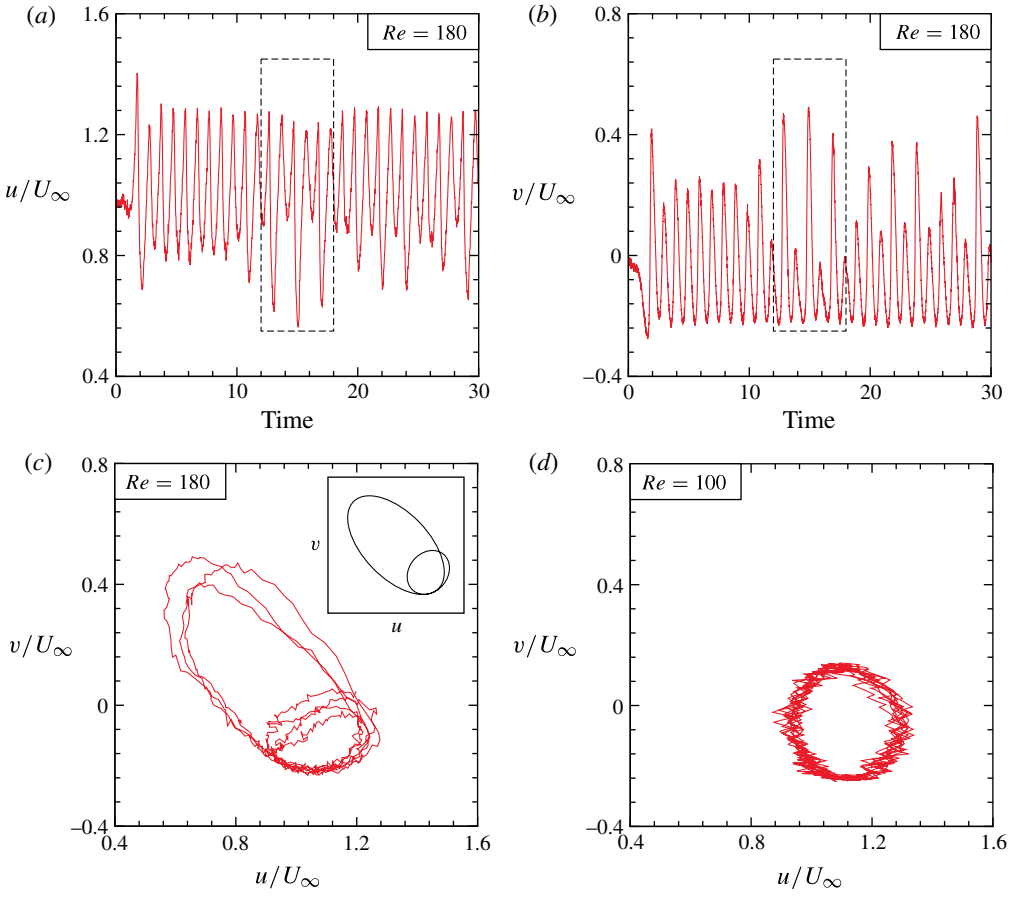

FIGURE 7. (Colour online) The phase plot of the velocity data in mode C transition. (*a*) Temporal variation of the u velocity. (*b*) Temporal variation of the v velocity. (*c*) The phase plot of the velocity data, which is shown in dashed boxes in plots (*a*) and (*b*). The velocity data are from XY-plane PIV experiments at $Re = 180$. (*d*) The phase plot for laminar two-dimensional flow at $Re = 100$. The data probe point in all experiments is $(u, v)(x/D, y/D) = (4.5, 1.5)$.

of the signal, which indicates that the signal has a period-doubling character. Period doubling can also be demonstrated in the phase plots of the velocity components.

Figure 7 presents the time variation of the u and v velocities and their plots for mode C transition, as well as the phase plot for $Re = 100$ for comparison. It can be seen that the u velocity signal also demonstrates the typical 'high-peak–low-peak' velocity pattern. The two velocity components are plotted against each other to obtain the phase plot of figure 7(*c*). There is a clear difference between the phase plots of mode C transition flow and the laminar two-dimensional flow at $Re = 100$. The latter demonstrates a clear single phase cycle. On the other hand, mode C flow shows two phase cycles, one within the other.

3.2.3. *Power spectra*

Spectrum analysis was also used to capture the frequency content and to identify the periodicity in the velocity signal of mode C transition. Figure 8 shows the power

https://doi.org/10.1017/jfm.2013.230 Published online by Cambridge University Press

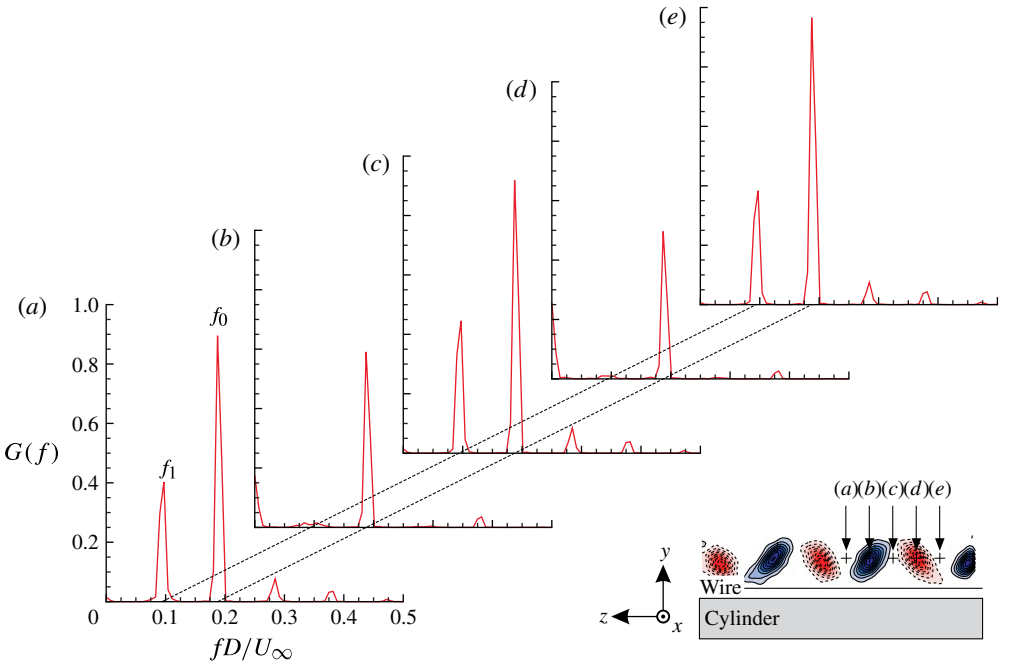

FIGURE 8. (Colour online) The spanwise variation of the v velocity spectra at $Re = 180$. The streamwise and transverse coordinates of the data probe points are $(x/D, y/D) = (4.5, 1.5)$.

spectra of cross-stream velocity signals obtained from YZ-plane PIV measurements. The Reynolds number is $Re = 180$ and the measurement plane is located at $x/D = 4.5$. The transverse coordinate of the data probe is $y/D = 1.5$. The spanwise coordinate was varied from (*a*) to (*e*) in figure 8 to evaluate the effect of spanwise location. The horizontal frequency axis is non-dimensionalized so that it represents the Strouhal number $St = fD/U_\infty$.

A clear peak at the von Kármán vortex shedding frequency, $f_0 \approx 0.19$, is seen in all spectra. It is evident from graphs (*a*), (*c*) and (*e*) that there is a second frequency component, $f_1 \approx 0.09$, which is approximately half of the von Kármán shedding frequency. The signals that have sharp peaks at f_1 in their spectra belong to the data probe locations that are halfway between the two secondary vortices. In conjunction with the discussion of velocity characteristics, the secondary frequency component f_1 can be thought as the reflection of the 'high-peak–low-peak' velocity profile of figure 4 in the frequency domain. Therefore, it indicates that the period of the secondary vortices in mode C transition is twice the shedding period of von Kármán vortices, $T_{secondary} = 2T_{shed}$.

The effect of the cross-stream location of the data probe point on the spectral characteristics is demonstrated in figure 9, which contains the two spectra from the upper and lower halves of the wake. Both spectra show clear peaks at the von Kármán shedding frequency, but only the upper spectra indicate a secondary subharmonic peak. Figure 9 also shows that the frequency ratio of the primary and secondary frequencies is approximately equal to 2 for the upper half of the wake. This suggests the existence of secondary vortices with a period-doubling nature.

https://doi.org/10.1017/jfm.2013.230 Published online by Cambridge University Press

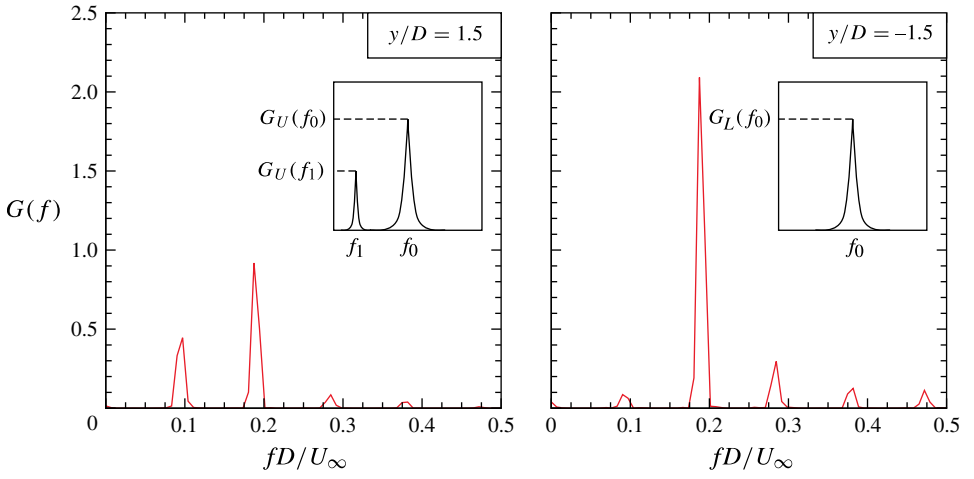

FIGURE 9. (Colour online) A comparison of the velocity spectra of the upper ($y/D = 1.5$) and lower ($y/D = -1.5$) halves of the wake. $Re = 180$. The streamwise coordinate of the data point is $x/D = 4.5$.

3.3. *Shedding frequency*

The vortex shedding frequency in mode C transition is calculated by determining the corresponding peaks in the power spectra of different experiments. Figure 10 shows the Strouhal number values at different Reynolds numbers. The results were plotted using the values of mode A and B transitions that were reproduced from Williamson (1996*a*) for comparison. Figure 10(*a*) shows the scatter of *St* values in the different experiments for mode C transition. The Strouhal numbers for mode C transition are calculated by simply averaging the values at the corresponding Reynolds number and the results are shown in figure 10(*b*).

Figure 10(*b*) shows a comparison of the Strouhal numbers for the non-wired and wired experiments with literature values. It is obvious that there is a deviation from the literature values in the measured Strouhal numbers for the non-wired case. When the literature values of Zhang *et al.* (1995) and the measurements are compared, the order of magnitude of this deviation is the same for the wired-cylinder case. Besides, one can see that the error bars indicated in figure 10(*b*) are relatively large, which is also reflected in the scatter of the Strouhal values as presented in figure 10(*a*). The Strouhal values are based on the frequencies determined from the power spectra, as presented in figure 8. A possible reason for the relatively large error bars is the limited number of shedding cycles in one experiment due to the finite length of the towing tank. However, the present experimental data for the non-wired and wired-cylinder cases are both internally consistent and consistent with the trend in the literature, showing that there is a reduction in the shedding frequency in mode C transition.

Therefore, one may conclude that the trend of the mode C experiments is in good agreement with the values of Zhang *et al.* (1995). Apparently, the wire changes the frequency characteristics of von Kármán vortices and it is likely that it suppresses the instability mechanisms that cause the discontinuities in the *St–Re* graph for the non-wired-cylinder flow.

https://doi.org/10.1017/jfm.2013.230 Published online by Cambridge University Press

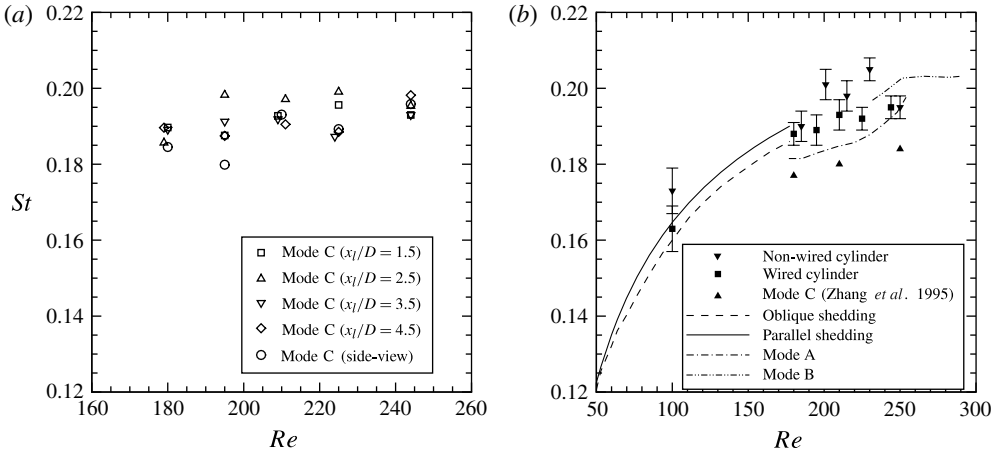

FIGURE 10. A comparison of the *Re*–*St* relationships for the single cylinder and the wired cylinder. The data for parallel shedding, oblique shedding and modes A and B are reproduced from Williamson (1996*a*). The *St* number for mode C transition is obtained from back-view and side-view PIV measurements. (*a*) The scatter of the *St* numbers of different mode C experiments. (*b*) A comparison of the non-wired and averaged *St* numbers of the wired experiments with literature values. The error bars indicate the frequency resolution of each corresponding spectrum.

3.4. *Breaking of symmetry*

The placement of a wire in the near wake of a cylinder obviously acts as a symmetry-breaking mechanism in the wake structure. This is evident in figure 11, where the time-averaged streamline topology $\overline{\Psi}$ for two Reynolds numbers is given. The streamlines are calculated using the time-averaged velocity components $\overline{u}$ and $\overline{v}$.

The $\overline{\Psi}$ patterns for the non-wired case indicate two symmetric swirl patterns in the near wake for both Reynolds numbers. From figure 11, it is clear that the size of these swirl patterns is decreasing with increasing Reynolds number. There is also a saddle point *S* located at the wake centreline at the downstream edge of the swirl patterns. The location of the saddle point actually corresponds to the most downstream point of the recirculation region.

In the wired cases, the two-symmetric-swirl-pattern topology is no longer seen. For $Re = 180$, the upper swirl region appears with a smaller size than its non-wired ($Re = 185$) counterpart. The same topology is seen for $Re = 225$, but with a swirl region slightly larger in size than for the non-wired ($Re = 230$) case. Another difference is that for the wired cases there is no apparent saddle point to identify. However, the major difference is in the lower part of the wake, where there is no clear time-averaged swirl pattern. It appears for the wired case that the upper swirl region is related to the diverted vorticity that extends beyond the wake centreline and smears the vorticity concentration of the lower shear layer. This mechanism seems to prevent the formation of a lower time-averaged swirl pattern during mode C transition. It needs to be remarked that the spanwise position of the measuring plane relative to the mode C structures is not known in these side-view experiments (see figure 1(*b*)). However, the aforementioned symmetry-breaking mechanism is observed in all experiments. Figure 14 shows the instantaneous spanwise vorticity patterns for two shedding cycles,

https://doi.org/10.1017/jfm.2013.230 Published online by Cambridge University Press

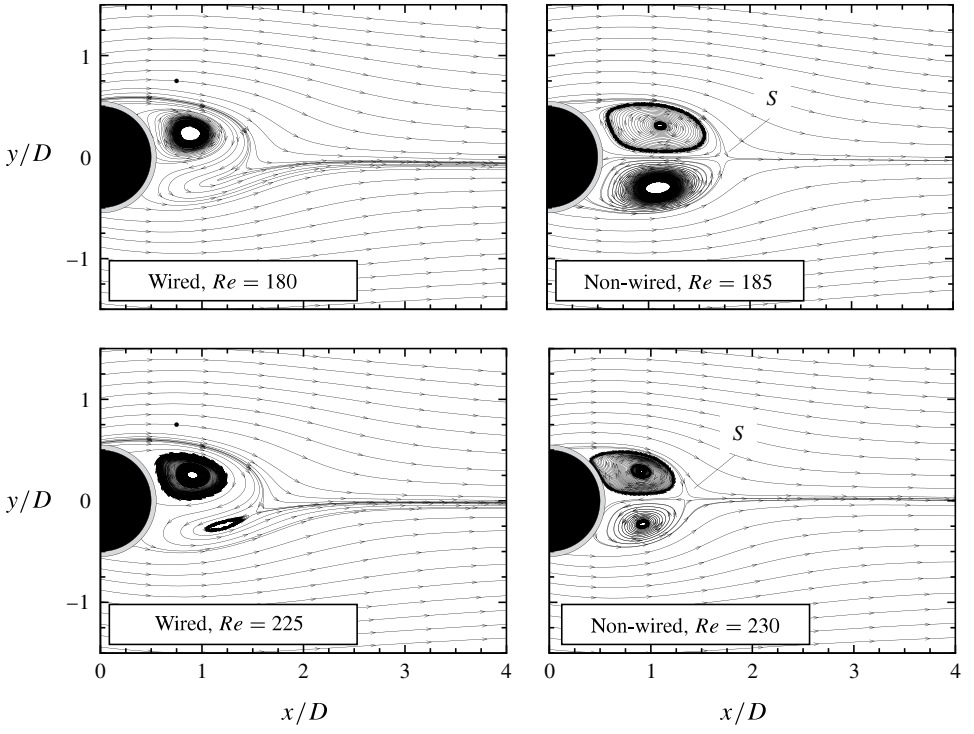

FIGURE 11. Time-averaged streamlines in the near wake of the cylinder.

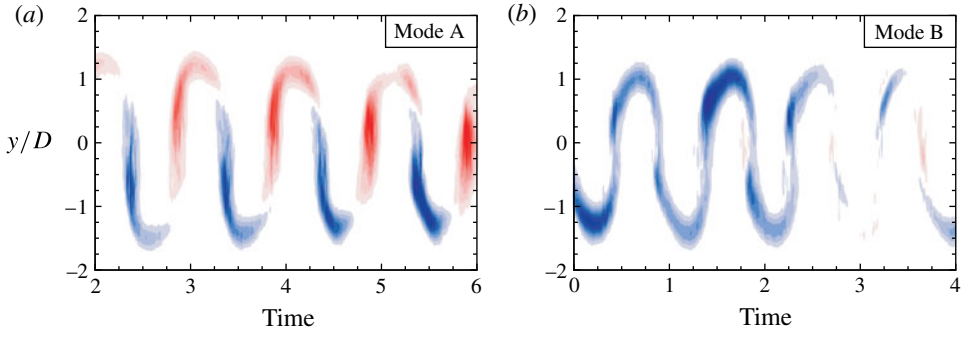

FIGURE 12. The time variation of the streamwise vorticity on the line $x/D = 4.5$ from back-view PIV experiments of the non-wired-cylinder wake at $Re = 185$ and $Re = 215$ for modes A and B, respectively. The time axis is non-dimensionalized with the corresponding shedding periods: (*a*) mode A; (*b*) mode B.

and clearly shows the difference in strength and structure between the upper and lower vortices during one shedding cycle and over two shedding cycles.

The symmetry-breaking effect of the wire can also be seen by comparing figures 12 and 13, which represent the streamwise vorticity component ω_x as a function of time for the non-wired and wired-cylinder wakes in mode A/B and mode C transition, respectively. In both figures, the streamwise vorticity component is evaluated along a

https://doi.org/10.1017/jfm.2013.230 Published online by Cambridge University Press

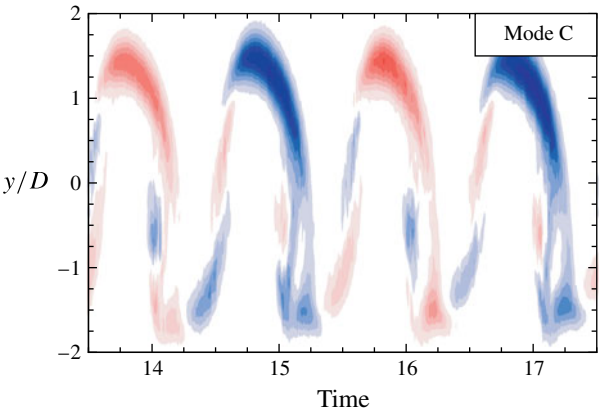

FIGURE 13. Time variation of the streamwise vorticity on the line $x/D = 4.5$ from back-view PIV experiments of the mode C wake at $Re = 180$. Time axis is non-dimensionalized with the corresponding shedding period.

vertical cross-stream line placed at downstream location $x/D = 4.5$ and through the centre of the secondary vortices. Therefore, contrary to the side-view experiments, in these back-view experiments (see figure 1(*c*)) the spanwise position relative to the mode C structures is exactly known. A similar approach has been employed by Carmo *et al.* (2008) to investigate the symmetry of transition modes in cylinder–cylinder interacting flows.

Figure 12 shows the symmetry characteristics of the non-wired-cylinder wake in the transition regimes associated with modes A and B at $Re = 185$ and $Re = 215$, respectively. The symmetry nature of the mode A wake is clearly seen in figure 12(*a*). The positive and negative vorticity appear in a symmetric manner, with a period of T_{shed}. From the colour contrast of the figure, one can also conclude that both the upper and lower streamwise vortices have almost equal vorticity contents. Hence, mode A can be characterized by

$$\omega_x(x, y, z, t) = -\omega_x(x, -y, z, t + T/2). \tag{3.1}$$

The symmetry of mode B can be observed in figure 12(*b*). The spanwise vorticity in mode B has the same sign on both sides of the wake during the vortex shedding cycle. Mode B is also T-periodic and can be characterized by

$$\omega_x(x, y, z, t) = \omega_x(x, -y, z, t + T/2). \tag{3.2}$$

For the wired-cylinder case, figure 13 clearly demonstrates that the wake undergoing a mode C transition is no longer symmetric with respect to the wake centreline and the vorticity field is $2T$-periodic, unlike modes A and B. Actually, the streamwise vorticity patterns change sign at every shedding period. In mode C transition, the temporal symmetry of the streamwise vorticity can therefore be described by

$$\omega_x(x, y, z, t) = -\omega_x(x, y, z, t + T). \tag{3.3}$$

A lot of studies have been performed on the effect of symmetry breaking of two-dimensional time-periodic wakes such as the von Kármán vortex street. For example, Blackburn, Marques & Lopez (2005) have investigated the effect of symmetries on three-dimensional transition modes in detail, using a Floquet stability analysis. From their study, it appears that an up–down symmetry breaking, and hence violation

https://doi.org/10.1017/jfm.2013.230 Published online by Cambridge University Press

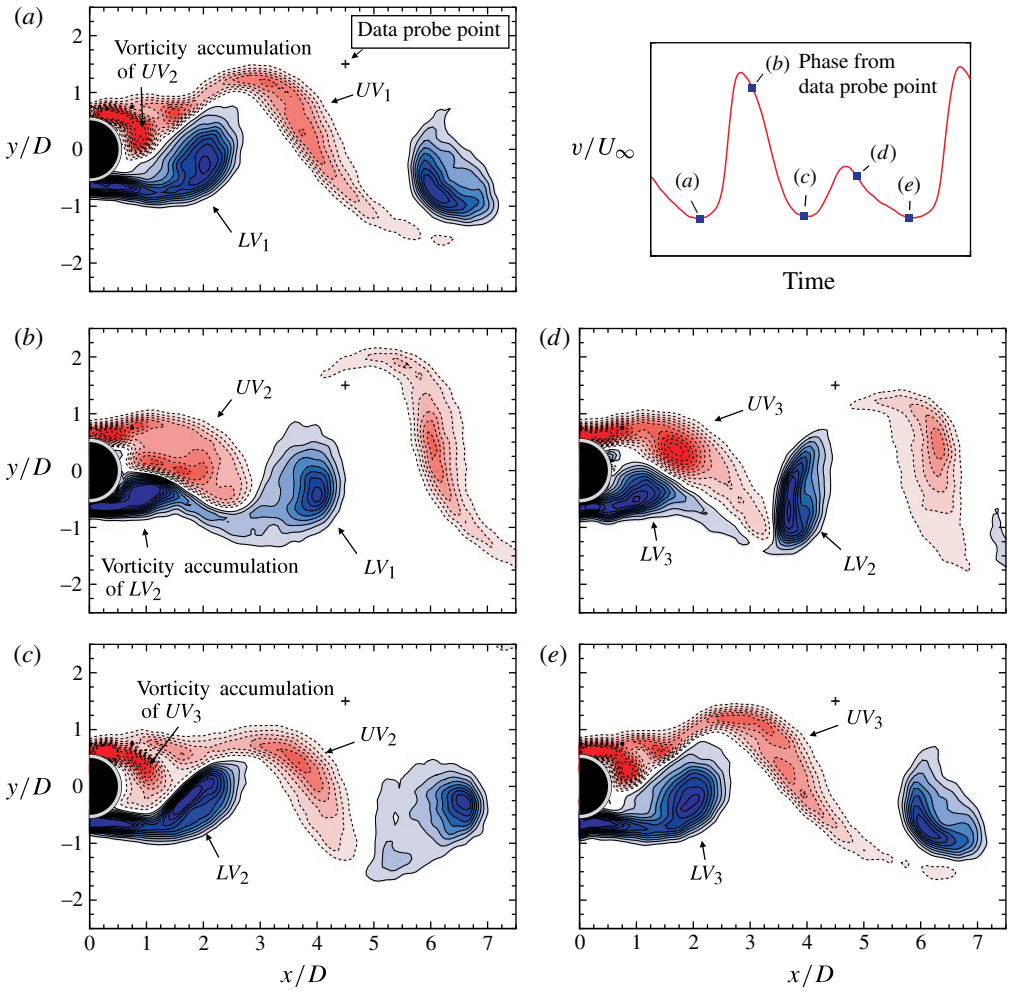

FIGURE 14. (Colour online) Instantaneous non-dimensional spanwise vorticity patterns $\omega_z D/U_\infty$ in the near wake of the cylinder. The contour levels are $|\omega_z|D/U_\infty = 0.4, 0.8, \ldots, 4$. The solid line and dashed line contours indicate positive and negative vorticity, respectively. The top right figure shows the phases of the vorticity fields with respect to the cross-stream velocity from the data probe point $(x/D, y/D) = (4.5, 1)$ at Reynolds number $Re = 180$. (*a*) $t = 0$; (*b*) $t = T_{shed}/2$; (*c*) $t = T_{shed}$; (*d*) $t = 3T_{shed}/2$; (*e*) $t = 2T_{shed}$.

of (3.2) as induced by the positioning of a thin wire in the vicinity of the cylinder, is a necessary prerequisite for period doubling as expressed in (3.3).

4. Vorticity patterns in the near wake

4.1. *Spanwise vorticity*

Figure 14 shows the evolution of spanwise vorticity in the near wake of the cylinder through two shedding periods for Reynolds number $Re = 180$. It demonstrates the period-doubling nature of mode C using the instantaneous spanwise vorticity ω_z snapshots. The phase information of the vortex shedding is obtained from the time signal of the vertical velocity component at point $(x/D, y/D) = (4.5, 1.5)$.

https://doi.org/10.1017/jfm.2013.230 Published online by Cambridge University Press

The image sequence starts with figure 14(*a*), which corresponds to the phase at which the upper vortex UV_1 is shedding. UV_1 is stretched and has two long vorticity braids. Meanwhile, the lower vortex LV_1 has a rather circular shape and is rolling up across the wake to cut the vorticity supply of UV_1. At this stage, the negative vorticity from the upper shear layer is directed into the base region. This accumulated vorticity later forms the subsequent upper vortex UV_2, indicated by an arrow in figure 14(*b*).

Figure 14(*c*) shows the vorticity patterns one shedding cycle after figure 14(*a*). Despite the similarities in the major vortical structures, some differences are still noticeable. First, the upper vortex UV_2 does not have long vorticity braids and is more compact than the preceding vortex UV_1. Secondly, the lower vortex LV_2 has a rather elliptic shape compared to LV_1. Finally, after a comparison of the snapshots figure 14(*a,c*), it looks as though the vorticity accumulation of the following upper vortex UV_3 uses a wider space in the base region than the preceding UV_2. At phase $t = 3T_{shed}/2$, the upper vortex UV_3 shows a clear vorticity concentration at around $x/D \approx 1.75$, with stretched vorticity braids around it. In this sense, UV_3 differs from its predecessor UV_2, which shows a vorticity spreading during the development stage (figure 14(*b*)). These observations show that the formation of primary von Kármán vortices in the mode C wake is not T-periodic but $2T$-periodic, as demonstrated in figure 14(*a,c,e*) for the upper vortices UV_1, UV_2 and UV_3, respectively.

4.2. *Streamwise vorticity*

To understand the temporal characteristics of the secondary vortices, instantaneous patterns of streamwise vorticity ω_x at cross-stream planes $x/D = 1.5$ and $x/D = 2.5$ are shown in figure 15, along with the corresponding von Kármán vortex shedding states for three independent experiments. The link between them is the phase relationship obtained from the vertical velocity signals at the intersection line of the two perpendicular planes, namely the XY-plane and the YZ-plane.

It is evident from the vorticity concentrations in the cross-stream planes that the secondary vortices are present in the wake, and that they originate from the very near wake of the cylinder. During the formation of the upper vortex at phase $t = 0$, there are two arrays of concentrated ω_x in the $x/D = 1.5$ plane. These vorticity arrays are aligned with the upper and lower shoulders of the cylinder and are out of phase with each other. Due to the stretching in the braid shear region, where the vorticity content of the secondary vortex is amplified, the mode C vortices are more clear in the $x/D = 2.5$ plane. The same vorticity structure is seen after $2T_{shed}$ in figure 15(*e*). At phase $t = T_{shed}$, similar vorticity arrays are seen, but the negative and positive vorticity structures are interchanged. The $2T$-periodic nature of the secondary vortices is apparent in the comparison of the vortex arrays at phases $t = 0, T_{shed}$ and $2T_{shed}$. The wake state at $t = 0$ is out of phase with the $t = T_{shed}$ state and in phase with the $t = 2T_{shed}$ state.

5. The development of period doubling in mode C transition

5.1. *The time evolution of the mode C vortices*

The formation process of mode C structures for a Reynolds number of $Re = 195$ throughout two shedding periods is illustrated in figures 17 and 18, which show top-view and side-view flow visualization sequences, respectively. The snapshots are synchronized qualitatively so that they represent the same vortex shedding phase and lead to the reconstruction of the feedback mechanism of mode C shedding. The illustration of the synchronization procedure is presented in figure 16. The main

https://doi.org/10.1017/jfm.2013.230 Published online by Cambridge University Press

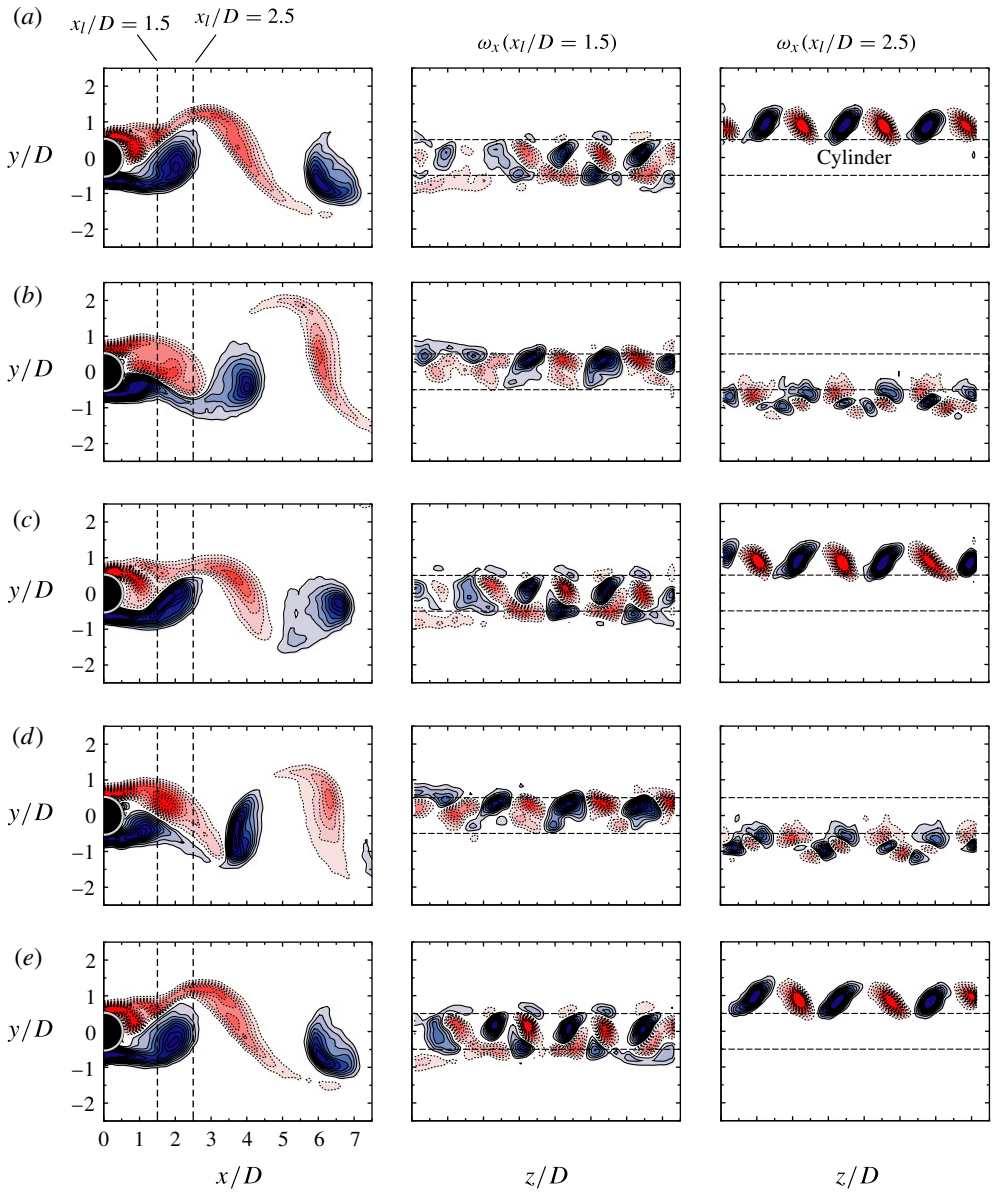

FIGURE 15. (Colour online) Instantaneous patterns of non-dimensional streamwise vorticity $\omega_x D/U_\infty$ in the near wake of the cylinder, measured at cross-stream planes $x_l/D = 1.5$ (middle column) and $x_l/D = 2.5$ (right column) at corresponding von Kármán vortex shedding phases (left column). The contour levels are $|\omega_z|D/U_\infty = 0.4, 0.8, \ldots, 4$ and $|\omega_x|D/U_\infty = 0.2, 0.4, \ldots, 2$. The blue (solid line) and red (dashed line) contours indicate positive and negative vorticities, respectively, at $Re = 180$. (*a*) $t = 0$; (*b*) $t = T_{shed}/2$; (*c*) $t = T_{shed}$; (*d*) $t = 3T_{shed}/2$; (*e*) $t = 2T_{shed}$.

cylinder diameter D is used as the reference length scale in the process. First, the images from the side-view experiments are scaled down in order to make the cylinder diameter equal in both experiments. Secondly, guide lines are drawn from the vortex locations in the top-view images. Thirdly, the corresponding side-view image is

https://doi.org/10.1017/jfm.2013.230 Published online by Cambridge University Press

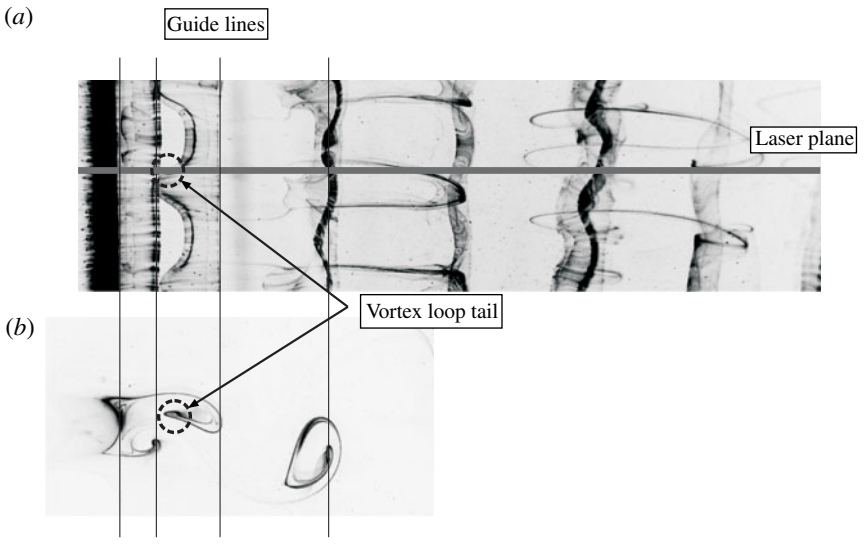

FIGURE 16. The synchronization of two independent flow visualization experiments. In the top figure, the probable location of the laser plane is shown. Guide lines are used to scale and synchronize the images.

determined using those guide lines for each top-view image. Finally, on the basis of the location of the vortex loop tails, the probable location of the laser plane of the side-view experiments is estimated in the top-view images.

The period-doubling nature of the process is illustrated in the phase diagram that is shown at the top right corner of figure 17. In this phase diagram, the letters correspond to the image numbers and indicate the vortex shedding phase. The initial image of the process, figure 17(*a*), is chosen such that it represents the approximate formation moment of the lower side von Kármán vortex, denoted as L_1. Likewise, the previously shed upper side von Kármán vortex is marked as U_1. This vortex U_1 shows spanwise waviness, which is the signature of the vortex loops originating from the upper vortex. Figure 18(*a–d*) reveals that the vortex loops are parts of the upper vortex, which are torn from it and stay in the base region. Figure 18(*a–d*) also show that these vortex loops originating from the upper vortex stay between the upper and lower vortices, affecting the near-wake dynamics. Moreover, these vortex loops are further stretched in the braid region, as seen in figure 18(*c–d*), and roll up to form streamwise vortex pairs from the sides of the loops, as shown in figure 17(*a–d*). During this half shedding period, the vortex loop tails of U_1 stay at a fixed position of approximately $\sim 0.5 - 0.7D$ from the rear end of the cylinder, while the rest of the vortex moves downstream.

The vortex loop tails of U_1 (see figure 18(*d*)), are apparently affecting the newly forming upper von Kármán vortex U_2 by initiating a spanwise waviness at the initial formation stage (see figure 17(*d*)). This wavy deformation in U_2 is amplified further in the recirculating region (see figure 17(*d–g*)) and forms vortex loops that are seen in figure 17(*g*). These vortex loop tails of U_2 appear at the spanwise position of the vortex loop heads of U_1 in the previous cycle. Therefore, figure 18(*g*) does not show any sign of an emerging vortex loop, as the laser plane is located at the vortex loop head instead of at a vortex loop tail.

https://doi.org/10.1017/jfm.2013.230 Published online by Cambridge University Press

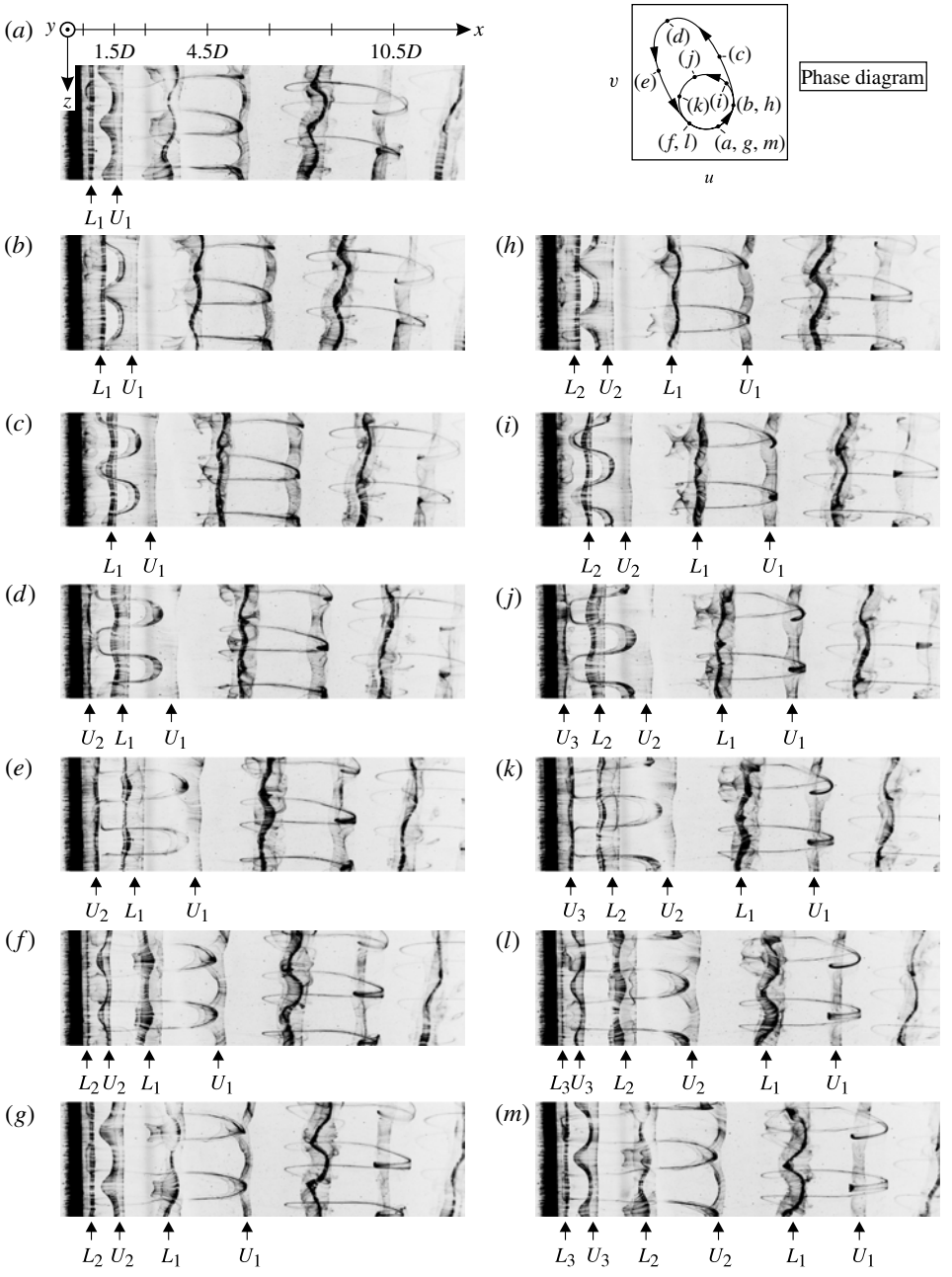

FIGURE 17. The formation and evolution of mode C structures in the wake of a wire-disturbed circular cylinder wake at a Reynolds number of $Re = 195$. The letters U and L indicate the upper-side and lower-side primary von Kármán vortices, respectively, and the subscripts show the indices of the corresponding vortices. The upper right diagram represents the vortex shedding cycles to which the representative images belong. (*a*) 0; (*b*) $(1/6)T_{shed}$; (*c*) $(2/6)T_{shed}$; (*d*) $(3/6)T_{shed}$; (*e*) $(4/6)T_{shed}$; (*f*) $(5/6)T_{shed}$; (*g*) T_{shed}; (*h*) $(7/6)T_{shed}$; (*i*) $(8/6)T_{shed}$; (*j*) $(9/6)T_{shed}$; (*k*) $(10/6)T_{shed}$; (*l*) $(11/6)T_{shed}$; (*m*) $2T_{shed}$.

https://doi.org/10.1017/jfm.2013.230 Published online by Cambridge University Press

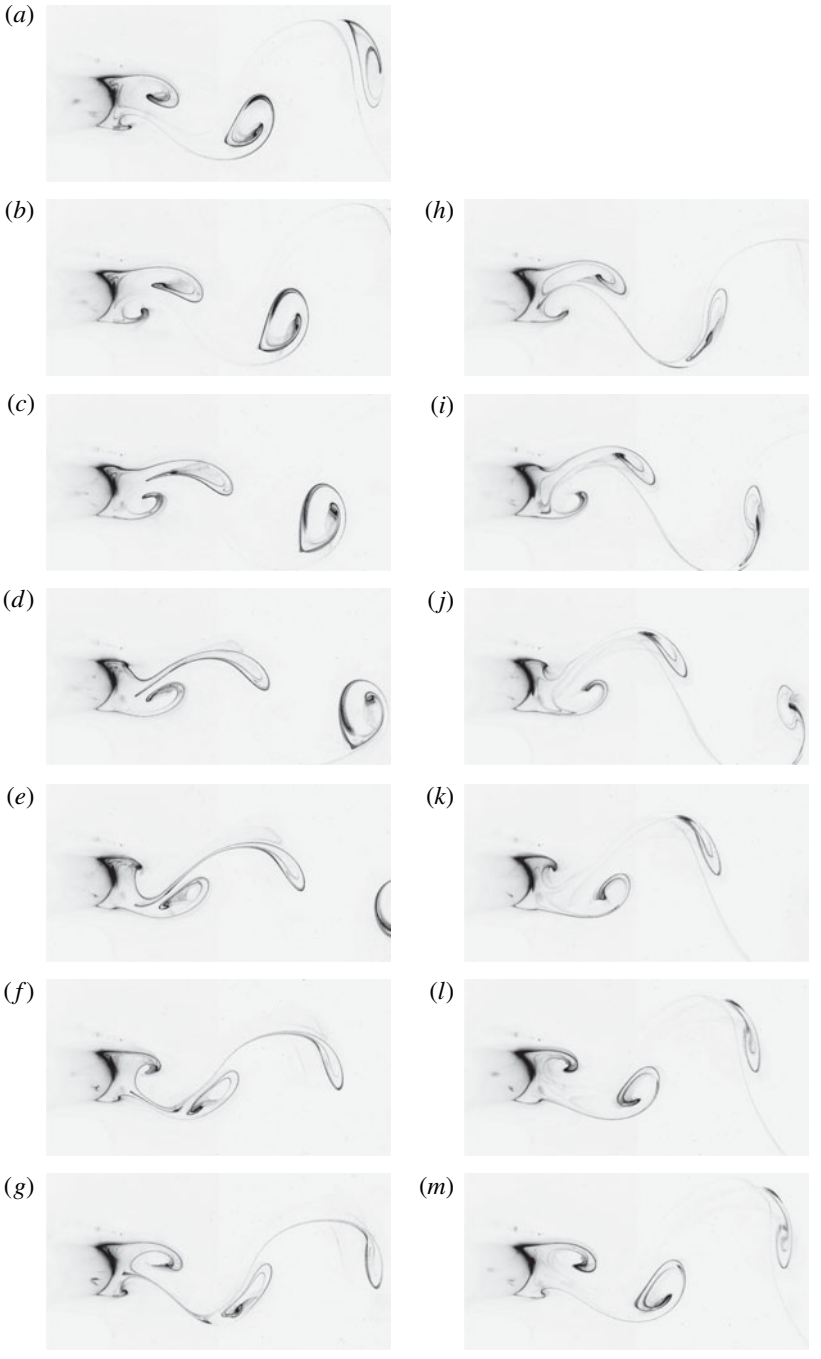

FIGURE 18. Side-view visualization snapshots showing the evolution of mode C structures at a Reynolds number of $Re = 195$. The snapshots represent approximately the same vortex shedding phase as in figure 17. (*a*) 0; (*b*) $(1/6)T_{shed}$; (*c*) $(2/6)T_{shed}$; (*d*) $(3/6)T_{shed}$; (*e*) $(4/6)T_{shed}$; (*f*) $(5/6)T_{shed}$; (*g*) T_{shed}; (*h*) $(7/6)T_{shed}$; (*i*) $(8/6)T_{shed}$; (*j*) $(9/6)T_{shed}$; (*k*) $(10/6)T_{shed}$; (*l*) $(11/6)T_{shed}$; (*m*) $2T_{shed}$.

https://doi.org/10.1017/jfm.2013.230 Published online by Cambridge University Press

In the first shedding period, the lower vortex L_1 has formed in a parallel way to the cylinder (see figure 17(*a,b*)), and preserves its shape until its encounter with the vortex loop tails of U_1, as shown in figure 17(*c*). Afterwards, L_1 continues to shed in a slightly wavy pattern. However, despite this waviness, the lower vortex L_1 does not develop any vortex loops and hence streamwise vortex pairs. Its waviness is initiated after approximately 1/3 periods – unlike, for example, the upper vortices U_2 and U_3, in which the waviness has started during the initial stages of formation.

The same physical process discussed above is also seen for the second part of the vortex shedding process in figure 17(*g–m*). The vortex loops of U_2 grow and form spanwise vortex structures, which in turn initiate the formation of vortex loops in U_3. The vortex loop tails of U_3 appear at the spanwise position of the vortex loop heads of U_2. Hence, the vortex loop tails of U_1 and U_3 occur at the same spanwise location: see figure 17(*a,m*), respectively. This type of occurrence effectively doubles the shedding period. Hence, an overall examination of the process suggests that the mode C instability is a self-sustaining process with a period of $T = 2T_{shed}$.

5.2. *The feedback mechanism between von Kármán vortices*

After the above discussion about the physical process of shedding, one may conclude that the period doubling is due to the feedback mechanism of streamwise vortices between two consequent upper vortices. In this section, this feedback process is discussed further using figure 19. The figure shows three instants from figure 17, each half a shedding period apart from each other and each zoomed into the near wake.

The growth of spanwise waviness and the formation of vortex loops can be illustrated as though a vortex line is being torn away from the primary von Kármán vortex and left to deform and stretch. The sketch on the left of figure 19 depicts vortex loop 1, which originates from the previously shed upper vortex U_1 and extends up to the cylinder. As shown in figure 18(*d*), vortex loop 1 lies in between the upper and lower vortices. The upstream convection of the vortex line, i.e. vortex loop 1, has different effects on the primary vortices L_1 and U_2.

First, the tails of vortex loop 1 induce a negative streamwise velocity on the lower vortex L_1 via Biot–Savart induction, as illustrated in figure 19. This perturbation makes the segments of L_1, which face the tails of vortex loop 1, move more slowly than the neighbouring segments, causing a wavy pattern along the lower vortex L_1. The slow-moving segments are at the same spanwise position as the perturbation source, i.e. the tails of vortex loop 1.

The second effect is on the newly forming upper vortex U_2. The tails of vortex loop 1 have already extended up to the cylinder, where they apparently effects the formation of U_2 at the initial formation stage by inducing a positive streamwise velocity perturbation (see the illustration in figure 19). Due to this perturbation, the segments of U_2 move slightly faster at the position of the vortex loop tails of U_1. The segments that are between the vortex loop tails move slowly and, at a later stage, form the new tails of vortex loop 2, as shown in the middle sketch of figure 19. At the later stage of the vortex shedding, the sides of the vortex loops will roll up and form a streamwise vortex array of mode C instability.

The middle sketch of figure 19 also represents the effects of the vortex loops on the formation of lower vortex L_2. Although the vortex loops of U_1 are still present in the near wake, they do not affect the L_2 at its initial formation stage. Considering that approximately 1.5 shedding periods have passed since the formation of vortex loop 1, it is likely that they are not strong enough to do so. The waviness of L_2 is initiated

https://doi.org/10.1017/jfm.2013.230 Published online by Cambridge University Press

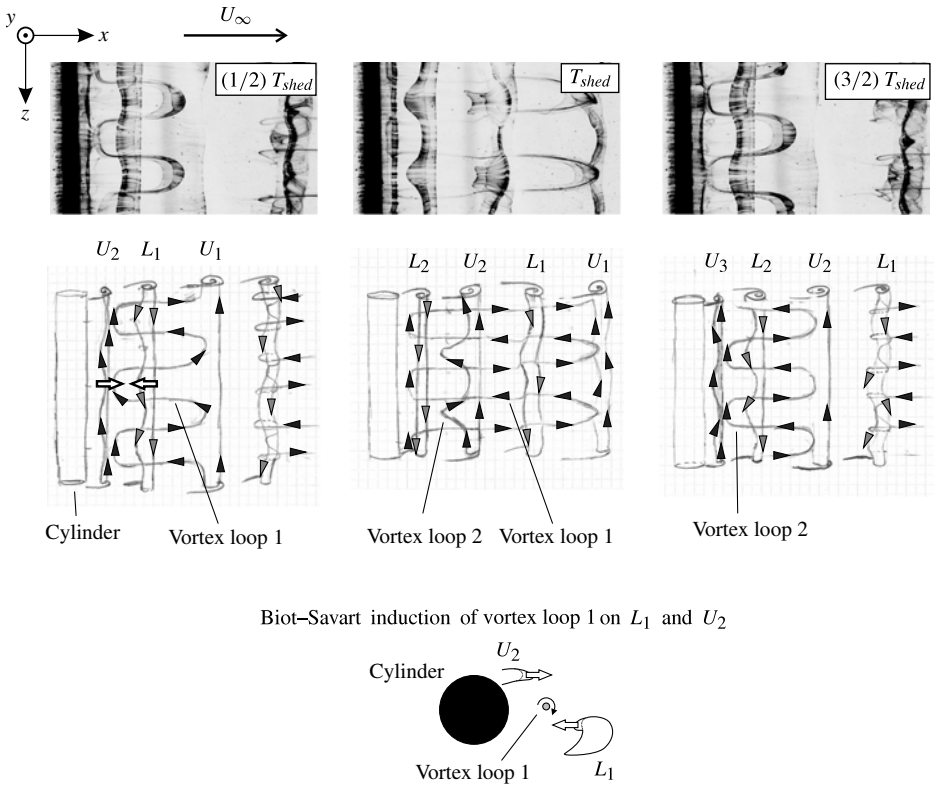

FIGURE 19. Sketches of the feedback mechanism of mode C vortex formation. The vortex line sketches are presented with the corresponding flow visualization snapshots at a Reynolds number of $Re = 195$. The flow visualization snapshots are zoomed into the formation region to make the near-wake vortex structures clear.

when it meets the tails of the following vortex loop 2, as presented in the sketch on the right of figure 19.

As discussed by Williamson (1996*a*), during the natural transition regime mode A, the feedback mechanism is set between the consecutive primary vortices, and this mechanism is the reason for the self-sustaining mode A vortex loops at the same spanwise position. On the other hand, for the mode C case, it is shown that the vortex loops of U_2 are not close enough to induce a perturbation on L_2 at the initial stage of the formation process. L_2 sheds parallel to the cylinder and does not show any spanwise waviness until it encounters the vortex loops of U_2. This encounter takes place when it is too late for the lower vortex to generate strong enough vortex loops within the next half-cycle. Therefore, L_2 cannot override the effect of *vortex loop* 2 on U_3. This process breaks the natural feedback mechanism of two consecutive primary vortices (lower and upper) in mode C transition and establishes a new feedback mechanism, which is apparently between the consecutive upper vortices only.

6. Concluding remarks

In conclusion, the current investigation aims to provide additional knowledge about the flow physics of the cylinder wake under the disturbance of a very thin wire. The

https://doi.org/10.1017/jfm.2013.230 Published online by Cambridge University Press

major consequence of placing a wire in the near wake of a cylinder is the triggering of mode C transition in the cylinder wake. Therefore, the flow behind a circular cylinder with a wire in the near wake has been investigated for Reynolds numbers of $Re = 165$–300 in the three-dimensional transition regime. The information about the flow physics has been obtained by flow visualization and PIV experiments. The experiments revealed that by placing a small control wire parallel to the cylinder at $x/D = 0.75$ and $y/D = 0.75$, the shedding pattern behind the cylinder changed dramatically and mode C transition appeared in the wake. Flow visualization images at $Re > 180$ revealed that mode C structures are found to have a spanwise wavelength of $\lambda_z \approx 2D$ and to appear at the same spanwise location at every two shedding periods.

The investigation of velocity–time signals, which are obtained from PIV experiments, revealed that they contain a W-shaped 'high-peak–low-peak' velocity profile. The reason for having this velocity profile is that secondary vortices change sign every shedding period. Due to this type of velocity profile, the u–v phase plot shows two phase cycles instead of one, indicating the period-doubling nature of the velocity signal.

Spectrum analysis showed that the 'high-peak–low-peak' velocity profile is reflected as a subharmonic frequency component in the frequency domain. Naturally, this subharmonic component is associated with the secondary mode C vortices, while the primary frequency peak is associated with von Kármán vortices. Primary frequency peaks in the spectrum denote the corresponding Strouhal numbers of mode C transition. In the experiments, when compared with mode A and B transitions, the Strouhal numbers for mode C are slightly lower than for modes A and B.

Investigation of both symmetry characteristics and instantaneous vorticity patterns showed that the mode C transition is $2T$-periodic rather than T-periodic. An analysis of the time evolution of the streamwise vorticity field revealed that the period of formation of von Kármán vortices does not change. However, due to the interaction with secondary vortices, their formation cycle shows a $2T$-periodic nature. That is, two shedding periods have to elapse for the same von Kármán vortex to be at the same location. Despite their T-periodic nature, the interaction mechanism of the upper and lower vortices during formation changes every period. The $2T$-periodic nature of the mode C wake is clearer when the time evolution of secondary vortices is analysed. The streamwise vorticity and rotation direction of the secondary vortices change sign every shedding period, causing the whole unsteady wake to become $2T$-periodic.

The secondary vortices in mode C transition are actually the vortex loops that originate from the upper vortex. These vortex loops are further stretched in the braid region and roll up to form streamwise vortex pairs from the sides of the loops. They are located between the upper and lower vortices and affect the near-wake vortex shedding process. Besides, it is shown that mode C instability exhibits feedback of streamwise vortices between the upper primary vortices only, which is contrary to the natural instability modes A and B. In mode C, the vortex loops are generated at the same spanwise position every two cycles. Therefore, it is concluded that period doubling in this type of flow is due to the feedback mechanism that appears between two upper vortices.

The present contribution mainly focuses on the general characteristics of mode C transition using top- and side-view visualization experiments, showing that in the Reynolds number range of $Re = 180$–300, the natural transition modes A and B are suppressed by the presence of a wire, and showing the formation and evolution of the mode C structures in the wake of a wire-disturbed cylinder flow for a Reynolds number of $Re = 195$. Side- and back-view PIV experiments are used to explore the

https://doi.org/10.1017/jfm.2013.230 Published online by Cambridge University Press

symmetry-breaking effect of the wire compared to the natural transition modes A and B, and to show the development of the streamwise vortices as a function of time. As indicated above, the secondary streamwise vortices in mode C transition originate from the primary upper vortices only, resulting in the typical $2T$-periodic nature of mode C. The energy transfer from the primary to the secondary vortices is analysed in detail elsewhere (see Yildirim, Rindt & van Steenhoven 2013). The origin of the instability for the natural transition modes A and B arises from an elliptic instability of the vortex cores for mode A and from a hyperbolic instability in the braid region for mode B (Williamson 1992, 1996*a*; Leweke & Williamson 1998; Thompson *et al.* 2001). The different spatial scales of the vortex cores and the braid regions are coupled to the typical wavelengths exhibited in mode A and B transitions. For mode C, this still remains an open question to be answered.

Acknowledgement

The authors would like to take the opportunity to thank the Netherlands Foundation for Fundamental Research on Matter (FOM) for supporting this research.

REFERENCES

BARKLEY, D. & HENDERSON, R. 1996 Three-dimensional Floquet stability analysis of the wake of a circular cylinder. *J. Fluid Mech.* **322**, 215–241.

BARKLEY, D., TUCKERMAN, L. S. & GOLUBITSKY, M. 2000 Bifurcation theory for three-dimensional flow in the wake of a circular cylinder. *Phys. Rev.* E **61** (5), 5247–5252.

BLACKBURN, H. M., MARQUES, F. & LOPEZ, J. M. 2005 Symmetry breaking of two-dimensional time-periodic wakes. *J. Fluid Mech.* **522**, 395–411.

BREDE, M., ECKELMANN, H. & ROCKWELL, D. 1996 On the secondary vortices in the cylinder wake. *Phys. Fluids* **8**, 2117–2124.

CARMO, B. S., SHERWIN, S. J., BEARMAN, P. W. & WILLDEN, R. H. J. 2008 Wake transition in the flow around two circular cylinders in staggered arrangements. *J. Fluid Mech.* **597**, 1–29.

DIPANKAR, A., SENGUPTA, T. & TALLA, S. B. 2007 Suppression of vortex shedding behind a circular cylinder by another control cylinder at low Reynolds number. *J. Fluid Mech.* **573**, 171–190.

GERRARD, J. H. 1966 The mechanics of the formation region of vortices behind bluff bodies. *J. Fluid Mech.* **25**, 401–413.

GERRARD, J. H. 1978 The wakes of cylindrical bluff bodies at low Reynolds number. *Phil. Trans. R. Soc. Lond.* A, *Math. Phys. Sci.* **288** (1354), 351–382.

GREEN, R. & GERRARD, J. 1993 Vorticity measurements in the near wake of a circular cylinder at low Reynolds numbers. *J. Fluid Mech.* **246**, 675–691.

HENDERSON, R. D. 1996 Secondary instability in the wake of a circular cylinder. *Phys. Fluids* **8** (6), 1683–1685.

HENDERSON, R. D. 1997 Nonlinear dynamics and pattern formation in turbulent wake transition. *J. Fluid Mech.* **352**, 65–112.

HONJI, H., TANEDA, S. & TATSUNO, M. 1980 Some practical details of the electrolytic precipitation method of flow visualization. *Rep. Res. Inst. Appl. Maths* **28**, 83–89.

KARNIADAKIS, G. E. & TRIANTAFYLLOU, G. S. 1992 Three-dimensional dynamics and transition to turbulence in the wake of bluff objects. *J. Fluid Mech.* **238**, 1–30.

KIEFT, R. N., RINDT, C. C. M., VAN STEENHOVEN, A. A. & VAN HEIJST, G. J. F. 2003 On the wake structure behind a heated horizontal cylinder in cross-flow. *J. Fluid Mech.* **486**, 189–211.

KUO, C. H., CHIOU, L. C. & CHEN, C. C. 2007 Wake flow pattern modified by small control cylinders at low Reynolds number. *J. Fluids Struct.* **23**, 938–956.

LEWEKE, T. & WILLIAMSON, C. H. K. 1998 Three-dimensional instabilities in wake transition. *Eur. J. Mech. (*B/*Fluids)* **17** (4), 571–586.

https://doi.org/10.1017/jfm.2013.230 Published online by Cambridge University Press

MAAS, W. J. P. M., RINDT, C. C. M. & VAN STEENHOVEN, A. A. 2003 The influence of heat on the 3D-transition of the von Kármán vortex street. *Intl J. Heat Mass Transfer* **46** (16), 3069–3081.

MARQUET, O., SIPP, D. & JACQUIN, L. 2008 Sensitivity analysis and passive control of cylinder flow. *J. Fluid Mech.* **615**, 221–252.

MITTAL, S. & RAGHUVANSHI, A. 2001 Control of vortex shedding behind circular cylinder for flows at low Reynolds numbers. *Intl J. Numer. Meth. Fluids* **35**, 421–447.

NOACK, B. R. & ECKELMANN, H. 1994 A global stability analysis of the steady and periodic cylinder wake. *J. Fluid Mech.* **270**, 297–330.

REN, M., RINDT, C. C. M. & VAN STEENHOVEN, A. A. 2006 Three-dimensional transition of a water flow around a heated cylinder at $Re = 85$ and $Ri = 1.0$. *J. Fluid Mech.* **566**, 195–224.

SHEARD, G. J., THOMPSON, M. C. & HOURIGAN, K. 2003 From spheres to circular cylinders: the stability and flow structures of bluff ring wakes. *J. Fluid Mech.* **492**, 147–180.

SHEARD, G. J., THOMPSON, M. C. & HOURIGAN, K. 2004 From spheres to circular cylinders: non-axisymmetric transitions in the flow past rings. *J. Fluid Mech.* **506**, 45–78.

SHEARD, G. J., THOMPSON, M. C. & HOURIGAN, K. 2005*a* Subharmonic mechanism of the mode C instability. *Phys. Fluids* **17** (111702).

SHEARD, G. J., THOMPSON, M. C., HOURIGAN, K. & LEWEKE, T. 2005*b* The evolution of a subharmonic mode in a vortex street. *J. Fluid Mech.* **534**, 23–38.

STRYKOWSKI, P. J. & SREENIVASAN, K. R. 1990 On the formation and suppression of vortex shedding at low Reynolds numbers. *J. Fluid Mech.* **218**, 71–107.

THOMPSON, M. C., LEWEKE, T. & WILLIAMSON, C. H. K. 2001 The physical mechanism of transition in bluff body wakes. *J. Fluids Struct.* **15**, 607–616.

UNAL, M. F. & ROCKWELL, D. 1988 On vortex formation from a cylinder. Part 1. The initial instability. *J. Fluid Mech.* **190**, 491–512.

WILLIAMSON, C. H. K. 1992 The natural and forced formation of spot-like 'vortex dislocations' in the transition wake. *J. Fluid Mech.* **243**, 393–441.

WILLIAMSON, C. H. K. 1996*a* Three-dimensional wake transition. *J. Fluid Mech.* **328**, 345–407.

WILLIAMSON, C. H. K. 1996*b* Vortex dynamics in the cylinder wake. *Annu. Rev. Fluid Mech.* **28**, 477–539.

YILDIRIM, I., RINDT, C. C. M. & VAN STEENHOVEN, A. A 2010 Vortex dynamics in a wire-disturbed cylinder wake for $Re = 100$. *Phys. Fluids* **22** (094101).

YILDIRIM, I., RINDT, C. C. M. & VAN STEENHOVEN, A. A 2013 Energy contents and vortex dynamics in mode C transition of wire-cylinder wake. *Phys. Fluids* **25** (054103).

ZHANG, H.-Q., FEY, U., NOACK, B. R., KONIG, M. & ECKELMANN, H. 1995 On the transition of the cylinder wake. *Phys. Fluids* **7** (4), 779–794.

https://doi.org/10.1017/jfm.2013.230 Published online by Cambridge University Press